

Correlation between unconventional superconductivity and strange metallicity revealed by operando superfluid density measurements

Ruozhou Zhang^{1,2†}, Mingyang Qin^{1,3†*}, Chenyuan Li^{4†}, Zhanyi Zhao^{1,5†}, Zhongxu Wei^{1,6}, Juan Xu¹, Xingyu Jiang^{1,5}, Wenxin Cheng^{1,5}, Qiuyan Shi^{1,5}, Xuewei Wang^{1,5}, Jie Yuan^{1,5,7}, Yangmu Li^{1,5}, Qihong Chen^{1,5,7}, Tao Xiang^{1,8}, Subir Sachdev^{4*}, Zi-Xiang Li^{1,5*}, Kui Jin^{1,5,7*}, and Zhongxian Zhao^{1,5,7}

¹*Beijing National Laboratory for Condensed Matter Physics, Institute of Physics, Chinese Academy of Sciences, Beijing 100190, China*

²*State Key Laboratory of Surface Physics and Department of Physics, Fudan University, Shanghai 200433, China*

³*Department of Materials Science and Engineering, Southern University of Science and Technology, Shenzhen 518055, China*

⁴*Department of Physics, Harvard University, Cambridge MA 02138, USA*

⁵*School of Physical Sciences, University of Chinese Academy of Sciences, Beijing 100049, China*

⁶*Department of Physics, Southern University of Science and Technology, Shenzhen 518055, China*

⁷*Songshan Lake Materials Laboratory, Dongguan, Guangdong 523808, China*

⁸*Beijing Academy of Quantum Information Sciences, Beijing, 100193, China*

†These authors contributed equally to this work.

*: qinmy@sustech.edu.cn; sachdev@g.harvard.edu; zixiangli@iphy.ac.cn; kuijin@iphy.ac.cn

Abstract

Strange-metal behavior has been observed in superconductors ranging from cuprates to pressurized nickelates¹⁻⁷, but its relationship to unconventional superconductivity remains elusive. Here, we perform *operando* superfluid density measurements on ion-gated FeSe films. We observe for the first time a

synchronized evolution of superconducting condensate and the strange-metal phase with electron doping. A linear scaling between zero-temperature superfluid density and the strange-metal resistivity coefficient is further established, which nails down a direct link between the formation of superfluid in the superconducting state and the scattering of carriers in the strange-metal normal state. Remarkably, the scaling also applies for different iron-based and cuprate superconductors despite their distinct electronic structures and pairing symmetries. Such a correlation can be reproduced in a theoretical calculation on the two-dimensional Yukawa-Sachdev-Ye-Kitaev model⁸ by considering a cooperative effect of quantum critical fluctuation and disorder. These findings indicate a fundamental principle governing superconducting condensation and strange-metal scattering in unconventional superconductors.

Main text

In the search for the microscopic mechanism of unconventional superconductors, a concerted effort has been directed toward understanding their normal states and how they link to superconductivity. It has been found that the normal state of various unconventional superconductors, e.g., cuprates^{1,2,9}, iron-based materials^{3,10}, magic-angle graphene⁷, and nickelates⁴⁻⁶ exhibits a linear-in-temperature (T -linear) resistivity extending to the low temperature. Such an anomalous transport behavior¹¹, termed as the strange metal, is acknowledged to be intimately related to unconventional superconductivity^{1,2,9,10,12}. However, despite extensive investigations over the past decades^{8,13-16}, the microscopic mechanism of strange-metal transport and the interplay between strange metal and superconductivity remain actively debated. One of the central questions is what the fundamental correlation between the strange-metal normal state and superconductivity is. To find clues for solving the puzzle, inspecting the crucial ingredient governing superconductivity across the strange-metal regime is immensely required.

One key parameter characterizing the superconducting state is the superfluid density,

ρ_s ($\equiv \lambda_{ab}^{-2} \propto n_s/m^*$, with λ_{ab} the in-plane magnetic penetration depth, n_s the superconducting carrier density and m^* the effective electron mass), which encodes the rigidity of quantum-mechanism phase of Cooper pairs, reflecting the resilience of pairing condensate against phase fluctuations^{17,18}. It has been widely observed in cuprates that the superconducting transition temperature (T_c) scales with ρ_{s0} [$\equiv \rho_s(T \rightarrow 0)$] (see e.g., Refs. ¹⁸⁻²⁰), which is beyond the standard Barden-Cooper-Schrieffer (BCS) scenario that T_c is determined by the pairing strength. More intriguingly, in overdoped cuprates such as $Tl_2Ba_2CuO_{6+\delta}$ (Tl2201) and $La_{2-x}Sr_xCuO_4$ (LSCO), the normal-state carrier density increases with hole doping, but both ρ_{s0} and the T -linear resistivity coefficient A_1 decrease^{13,14}, suggesting a pivotal role of the strange-metal state in the pairing condensate. Consequently, establishing a quantitative relationship between ρ_{s0} and A_1 , and exploring to what extent it can be applied to unconventional superconductors are of vital importance in understanding the essential physics underlying the connection between unconventional superconductivity and the strange metallicity, and establishing a unified theoretical framework of unconventional superconductors. However, the great challenges involve manipulating superconductivity minutely across the strange-metal regime and obtaining precise ρ_{s0} data in an efficient way.

For LSCO, the systematic evolution of ρ_{s0} with T_c in the overdoped regime has been revealed by Božović *et al*¹⁸, based on massive data from over 2000 films prepared within about 12 years. Other than chemical substitution methods, the ionic liquid gating (ILG) technique is an approach that can continuously tune T_c of a single sample by virtue of either electrostatic or electrochemical effects²¹. FeSe, a prototype iron-based superconductor with the simplest crystal structure containing only the Fe-Se layer, has shown its unique compatibility with the ILG technique, i.e., the almost fivefold enhancement of T_c under gating²². Importantly, the strange-metal state of FeSe films with T -linear resistivity, linear-in-field (H) magnetoresistance, and H/T scaling of magnetoresistance was unambiguously identified, and its evolution with ionic-liquid gating was also disclosed in our previous work¹⁰.

Here, we perform *operando* ρ_s measurements by the two-coil mutual inductance (TCMI) technique on the ion-gated FeSe films, with T_c finely tuned in a wide range of approximately 11 to 43 K in a single sample. With this high-efficiency approach, we uncover a systematic dependence of T_c on ρ_{s0} for the iron-based superconductors, i.e., $T_c \propto \rho_{s0}^{0.55 \pm 0.11}$. Intriguingly, we find that the superfluid condensate keeps in lockstep with the strange-metal phase during the gating process. A linear correlation between ρ_{s0} and A_1 , i.e., $\rho_{s0} \sim A_1$, is further quantified, which also works for iron pnictides and overdoped cuprates. Such a relation is well captured by the two-dimensional Yukawa-Sachdev-Ye-Kitaev (2d-YSYK) model with a spatially disordered fermion-scalar coupling and potential disorder. Our findings reveal the quantitative connection between unconventional superconductivity and the strange metallicity, which may be common to the physics of different unconventional superconductors. (In this text, the symbols " \propto " and " \sim " denote a proportional relationship and a generic linear relationship allowing for a constant intercept, respectively.)

FeSe films ($T_c \approx 11$ K) with thicknesses of 60 ± 5 nm were deposited on (001)-oriented LiF substrates with size of 5×5 mm² by the pulsed laser deposition technique. The x-ray diffraction measurements confirm the high-quality (00 l) oriented growth of the film (Supplementary Section 1). The pristine films were loaded in our ILG device as schematically shown in Fig. 1a. An ionic liquid *N,N*-diethyl-*N*-(2-methoxyethyl)-*N*-methyl ammonium bis(trifluoromethylsulfonyl)imide (DEME-TFSI) was used as the dielectric, covering both the FeSe film and the gate electrode. Under a positive gate voltage, the H⁺ ions in the ionic liquid enter the FeSe film, which has been evidenced by the time-of-flight secondary ion mass spectroscopy measurement¹⁰. Such an electron doping effect brings forth a transition in the carrier type of FeSe from the coexistence of electrons and holes to high-density electrons only (Supplementary Section 2), which is accompanied by an enhancement of T_c to approximately 40 K (Refs. ^{10,22}).

The superfluid density, $\rho_s \equiv \lambda_{ab}^{-2}$, is difficult to be accurately measured since λ_{ab} is typically thousands of angstroms. The TCMI technique is a suitable method to obtain the absolute value of ρ_s of superconducting films, which has attracted increasing

attention due to its high sensitivity and flexibility¹⁸. In order to in situ monitor the evolution of ρ_s of FeSe films, the ILG device was integrated into a homemade transmission-type TCMI apparatus that consists of a drive coil and a pickup coil²³. Figure 1c shows the temperature-dependent pickup coil voltage, $V = V_x + iV_y$, for a gated state with $T_c \approx 43$ K. The real component, V_x , undergoes a rapid drop around T_c , originating from the diamagnetic effect of the screening supercurrent (see the calculated current distribution in the FeSe film in Fig. 1b). Correspondingly, the imaginary component, V_y , shows a sharp dip, resulting from the energy dissipation²⁴. The absolute value of ρ_s can be accurately extracted from V by employing a self-developed fast wavelet collocation (FWC) method²⁵, as shown in Fig. 1d (see Supplementary Sections 3 and 4 about the device configuration and the λ_{ab} measurements).

By minutely tuning the superconductivity of FeSe film via the ILG technique, a systematic evolution of the diamagnetic responses is obtained. It is shown that the diamagnetic signals exhibit a quasi-parallel shift to high temperature with gating (Supplementary Sections 5). Importantly, each curve exhibits only a single transition, confirming the bulk modulation of the superconductivity. Figure 2a shows the extracted temperature dependence of superfluid density, $\rho_s(T)$, for all gated states. A common feature is the flattening of ρ_s at low temperatures, which becomes more prominent for higher- T_c states. Such a feature has been observed in iron-based superconductors, e.g., $\text{Ba}_{1-x}\text{K}_x\text{Fe}_2\text{As}_2$ (Ref. ²⁶), noted as an indication of the nodeless pairing gap. We fit the $\rho_s(T)$ data with nodeless gap equation, i.e., $\rho_s(T) = \rho_{s0}(1 - Ce^{-\Delta_{\min}/k_B T})$, where Δ_{\min} is the minimum gap size, k_B is the Boltzmann constant, C is the numerical parameter, and ρ_{s0} is the superfluid density at zero-temperature limit, which works well at low temperatures (see Fig. 2b). We note that the ρ_{s0} value of the pristine FeSe film ($1.09 \pm 0.09 \mu\text{m}^{-2}$) is consistent with the value of FeSe_{1-x}Te_x film ($1.29 \pm 0.11 \mu\text{m}^{-2}$) measured by the scanning SQUID microscope²⁷, but is about 1/6 of the bulk FeSe ($6.25 \mu\text{m}^{-2}$, Ref. ²⁸). Such a relatively low ratio of thin film to bulk crystal seems ubiquitous in unconventional superconductors, e.g., 1/5 for $\text{Ba}(\text{Fe}_{1-x}\text{Co}_x)_2\text{As}$ (Refs. ^{29,30}) and 1/9 for $\text{YBa}_2\text{Cu}_3\text{O}_{6+y}$ (Refs. ^{20,24}), which was attributed to the relatively strong quantum phase fluctuations³¹ and/or disorder effect³² in thin films.

With the systematic ρ_s data, we explore the dependence of T_c on ρ_{s0} , which exhibits a simple power-law behavior (Fig. 2c), that is, $T_c = \gamma \rho_{s0}^{0.55 \pm 0.11}$, where γ is a numeric parameter. Here, the uncertainty in the power-law exponent is mainly caused by the error bars of the T_c value, i.e., ΔT_c (see Fig. 1c), which may be associated with the relatively inhomogeneous modulation of the superconductivity by ionic-liquid gating, or the strong superconducting fluctuations of FeSe²⁸. Such a relationship between T_c and ρ_{s0} holds well against different gap symmetries used to extract ρ_{s0} (Supplementary Section 6). We emphasize that this is the first systematic $T_c(\rho_{s0})$ scaling established in iron-based superconductors, benefiting from our high-efficiency *operando* measurements.

It was suggested that a power-law index ≈ 0.5 might occur in the dirty limit of a d -wave BCS superconductor^{33,34}. However, such a simple ‘dirty’ BCS picture could not quantitatively explain our observations, since our data unambiguously violate the Homes’ law, i.e., $\rho_{s0} \propto \sigma_{dc} T_c$ (where σ_{dc} is the normal-state conductivity measured closed to T_c) (see Supplementary Section 7), that typically holds for a dirty BCS superconductors owing to the Glover–Ferrell–Tinkham sum rule^{18,35,36}. We noticed that the $T_c \propto \rho_{s0}^{0.5}$ relation was also observed near the critical doping where superconductivity vanishes^{18,37} and was attributed to the critical quantum phase fluctuations^{20,38,39}. Besides, a similar scaling relation is found by our 2d-YSYK modeling of a quantum critical metal with fermion-scalar Yukawa couplings and potential disorder (Fig. S13b in Supplementary Section 14). Although further studies are needed to determine the mechanism responsible for the power-law behavior observed here, the strong correlation between T_c and ρ_{s0} demonstrates that phase rigidity plays a dominant role in determining T_c of ion-gated FeSe, in contrast to the standard BCS paradigm where T_c is bounded by the temperature at which Cooper pairs form. This is corroborated by large ratios of $(T_c/T_F, \Delta_{\min}/E_F) \approx (0.11, 0.23)$ for samples with $T_c > 39$ K ($E_F = k_B T_F$ is the effective Fermi energy derived from ρ_{s0}), indicating that ion-gated FeSe locates in the BCS-Bose-Einstein condensation (BEC) crossover regime²⁸ (Fig. 2d).

More importantly, by displaying the systematic ρ_s data in the phase diagram with varying electron doping and temperature, we are able to trace the evolution of the superconducting condensate with the normal-state resistivity (Fig. 3a). Intriguingly, we find that the magnitude of the superfluid density and the strength of the strange-metal scattering (dissipation) are synchronously enhanced with electron doping, which is accompanied by the similar increasing trends for T_c (see the gray circles and gray squares) and the upper bound temperature of T -linear resistivity (T_1 defined in the inset of Fig. S7). These observations provide strong evidence that the formation of superfluid condensation is linked with the strange-metal normal state, which is compatible with the scenario recently proposed in overdoped cuprates that superfluid condensation originates from incoherent carriers contributing to the strange-metal transport^{13,40}. To the best of our knowledge, such a visualized description of the interplay between unconventional superconductivity and the strange metallicity has not been established before.

Figure 3b shows both ρ_{s0} and A_1^\square as a function of electron doping for the ion-gated FeSe film, where A_1^\square is the T -linear resistivity coefficient normalized by the distance between adjacent superconducting layers. Strikingly, ρ_{s0} tracks A_1^\square closely for all gated states, which unambiguously points to a linear correlation between ρ_{s0} and A_1^\square , i.e., $\rho_{s0} = \alpha \tilde{A}_1^\square$ with $\alpha = 0.43 \pm 0.02 \mu\text{m}^{-2} \Omega^{-1}\text{K}$ (Fig. 3c). Here, a constant has been subtracted from A_1^\square , namely $\tilde{A}_1^\square = A_1^\square - A_0$, where $A_0 = 17.5 \Omega \text{K}^{-1}$ represents the non-zero extrapolation of A_1 to $\rho_{s0} = 0 \mu\text{m}^{-2}$ or $T_c = 0 \text{K}$ (Ref. ¹⁰). Note that with the error bars taking into account, the linear relationship is the best fit to the ρ_{s0} versus A_1^\square data (Supplementary Section 9).

To figure out to what extent the linear scaling of ion-gated FeSe is applied to other superconducting materials, we collect the ρ_{s0} and A_1^\square data from previous reports (see the original data in Supplementary Section 11). Systematic A_1^\square data of electron-doped cuprate $\text{La}_{2-x}\text{Ce}_x\text{CuO}_4$ (LCCO) have been obtained on composition-spread films⁹, but

corresponding ρ_{s0} data are lacking due to the difficulty of accurately characterizing the local superfluid density. The calculated upper bound of ρ_{s0} and measured A_1^\square of magic-angle graphene follow the similar trend as doping varies^{7,41}, but systematic superfluid measurements are required to obtain a quantitative relation. In spite of large error bars, the data of iron-pnictide superconductors BFCA reside in the linear trend. For overdoped Tl2201, ρ_{s0} and A_1^\square were found to decrease in tandem with the increase of hole doping, as pointed out by Philips *et al.*⁴⁰, which is similar to our finding and implies a linear relation despite the relatively scarce data points. For overdoped LSCO, although the strong correlation between ρ_{s0} and A_1^\square still persists, a quantitative relationship cannot be pinned down due to the large uncertainty of the A_1^\square data (see Supplementary Section 12). The data points of A_1^\square and ρ_{s0} are well fitted by a linear relation within error bar, particularly in the regime of $T_c < 12\text{K}$. To summarize, we plot the $\rho_{s0}/(\rho_{s0})^{\max}$ versus $\tilde{A}_1^\square/(\tilde{A}_1^\square)^{\max}$ relationship in Fig. 4a (the superscripts max refer to the maximum values in the literature), which suggests a linear scaling behavior that captures the common relation between ρ_{s0} and A_1^\square among different superconducting systems.

The similarity of ion-gated FeSe and overdoped cuprates revealed by the ρ_{s0} versus A_1^\square relation is surprising because they are distinct in many aspects. In overdoped cuprates, the normal-state carrier density exhibits an anticorrelation with ρ_{s0} as the hole doping varies^{13,18}. Whereas in FeSe, the ionic-liquid gating gives rise to the enhancement in ρ_{s0} , accompanied with an increase in the electron density and a decrease in the hole density (Supplementary Section 2). FeSe's nodeless gap (see e.g., Ref.²⁸ and Fig. 2b) also indicates that it differs from the cuprates in the pairing symmetry. Hence, the universal scaling shown in Fig. 4a indicates a fundamental link between superconducting condensation and the strange-metal scattering in unconventional superconductors. Since ρ_{s0} is a crucial ingredient determining T_c in unconventional

superconductors^{18-20,37}, it may also provide a natural explanation of the scaling relation between A_1^\square and T_c ubiquitously observed during the last decades (see e.g., Refs. ^{1,2,9,40}).

To gain further insights into the correlation between ρ_{s0} versus A_1 , we perform the calculations based on a universal theory of strange metals, captured by a model involving metals of fermions coupled to quantum critical order-parameter scalars, dubbed as the 2d-YSYK model. The recent work unambiguously shows that the 2d-YSYK model^{8,42,43} with spatially random Yukawa couplings exhibits the T -linear resistivity of strange metals, and can display the instability from the strange metal to the superconductivity⁴² (see details in Supplementary Section 14). Strikingly, by varying the renormalized boson mass M and the potential disorder stimulatingly, a linear ρ_{s0} versus A_1 relation is reproduced (Fig. 4b). Here, M is changed to tune the distance to the putative quantum critical point (QCP)⁴², which is a basic effect of doping or gating in experiments. Notably, such a choice of model parameters is consistent with the fact that doping or gating also inevitably alters the amount of disorder, as evidenced by the evolution of the residual resistivity ratio (Supplementary Section 13) and was highlighted by recent studies of overdoped cuprates (see e.g., Refs. ^{44,45}). Disorder is a strongly relevant perturbation to clean quantum-criticality, which can explain the applicability of the 2d-YSYK theory to relatively clean samples^{42,46}. The agreement between the theoretical calculations and the experimental data thus suggests a comprehensive consideration of quantum criticality and disorder provides a promising route for deciphering the interplay between strange metallicity and superconductivity in unconventional superconductors. As a consequence, combining the theoretical calculation on 2d-YSYK model, our experimental findings bring us closer to a unified understanding of the normal-state strange metal and superconductivity in unconventional superconductors.

In addition, a non-zero extrapolation of A_1^\square to $\rho_{s0} = 0 \mu\text{m}^{-2}$ or $T_c = 0 \text{ K}$ is seemingly ubiquitous in overdoped cuprates including LSCO and Bi2201 (Ref. ¹⁴), which is witnessed from the difference of the boundaries of superconducting dome (p_{sc}) and the strange-metal phase (p_{sm}) in the T versus doping phase diagram, as depicted in

Supplementary Section 15. This may stem from the suppression of superconductivity between p_{sc} and p_{sm} due to pair breaking⁴⁷ or the presence of competing orders⁴⁸. Besides, it was suggested that the multi-orbital effect in iron-based superconductors, which involves orbital-dependent quasi-particle spectral weights in the normal state and orbital-selective pairing in the superconducting state⁴⁹, could contribute to the residual A_1^\square (Ref. ¹⁰). Whether these scenarios could account for the residual A_1^\square remains to be investigated.

Acknowledgments

The authors would like to thank Dung-Hai Lee and Yuji Matsuda for fruitful discussions. This work was supported by the National Key Research and Development Program of China (Grants Nos. 2021YFA0718700, and 2022YFA1603903), the National Natural Science Foundation of China (Grants Nos. 12225412, 11927808, and 12274439), the CAS Project for Young Scientists in Basic Research (Grant No. 2022YSBR-048), the Key-Area Research and Development Program of Guangdong Province (Grant No. 2020B0101340002), the Beijing Nova Program of Science and Technology (Grant No. 20220484014).

Author contributions

K.J. and Z.X.Z. conceived the project. M.Y.Q. and Z.X.L. supervised the project. M.Y.Q. and R.Z.Z. designed the two-coil mutual inductance measurement device. R.Z.Z. and M.Y.Q. developed the fast wavelet collocation method for extracting the magnetic penetration depth from the pickup coil voltage. R.Z.Z. and M.Y.Q. performed the ionic liquid gating and the superfluid density measurements, with help from J.X., W.X.C., X.W.W. and Q.Y.S.. C.Y.L. performed the calculations based on the two-dimensional YSYK model, with the guidance of S. S.. Z.Y.Z. synthesized the FeSe films. M.Y.Q. and R.Z.Z. analyzed the experimental data, with assistance from Z.X.W., X.Y.J., J.Y., Y.M.L., and Q.H.C.. T.X., Z.X.L. and S.S. contributed to the theoretical discussions. R.Z.Z., M.Y.Q., C.Y.L., S.S., Z.X.L. and K.J. wrote the manuscript with input from all authors.

Competing interests

The authors declare no competing interests.

Data availability

Source data are provided with this paper. All other data that support the findings of this study are available from the corresponding authors upon reasonable request.

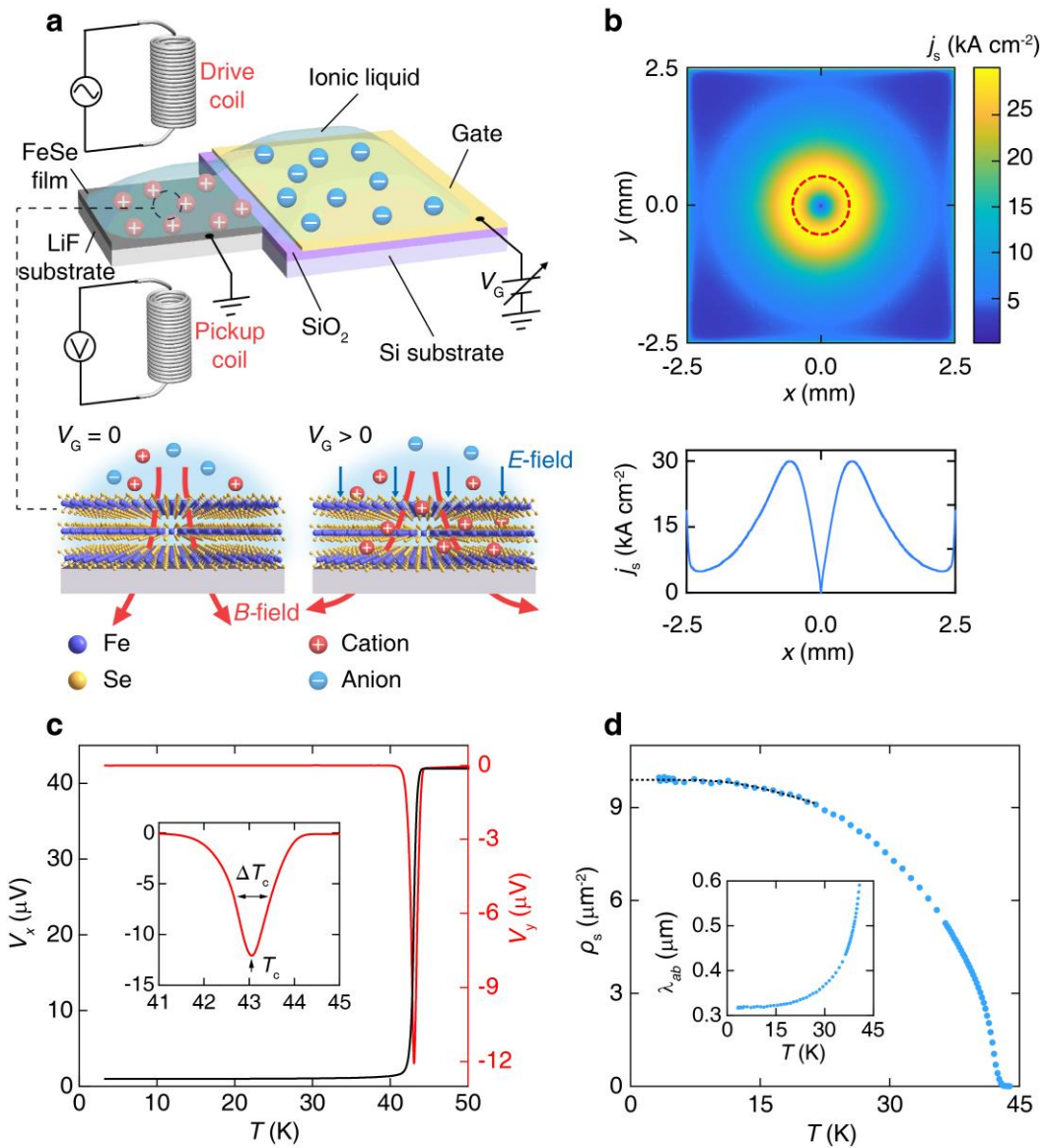


Fig. 1 | Operando superfluid density measurements on the ion-gated FeSe film. a, Schematic of a typical ILG device and the TCMI measurement scheme. The ILG device consists of a FeSe film and a gate electrode, with the ionic liquid DEME-TFSI covered. A positive gate voltage (V_G) is applied between the gate electrode and the film to induce the electrochemical protonation. A drive coil and a pickup coil are mounted on opposite sides of the ILG device for in-situ measurements of the diamagnetic response of the sample. The lower picture shows the enlarged schematic of the ion-gated FeSe. Under a positive V_G , the cations in the DEME-TFSI will enter the FeSe film, resulting in an enhancement of the superfluid density. Consequently, the diamagnetic response becomes stronger, from which the evolution of superfluid density with ionic-liquid gating can be extracted. **b,** Top view of the induced screening current density, j_s , for the

ion-gated FeSe film with $T_c \approx 43$ K, calculated using the FWC method²⁵ (Supplementary Section 4). The red dashed line shows the position of the drive coil. The lower panel shows the cut at $y = 0$. **c**, Temperature dependence of the pickup coil voltage, $V = V_x + iV_y$, for a gated state with $T_c \approx 43$ K. The sudden drop of V_x (black line) around T_c reflects the strong diamagnetism of the superconducting state. Accordingly, V_y (red line) shows a dip and its full width at half maximum is smaller than 1 K, indicating good homogeneity of superconductivity²⁰. Inset: Zoom-in of the V_y versus T curve. T_c and ΔT_c are the position and the full width at half maximum of the dip, respectively, following the definitions in Ref. ²⁴. **d**, Temperature-dependent superfluid density, $\rho_s(T)$, extracted from the pickup coil voltage in **c**. The dashed line represents the nodeless-gap fit (Supplementary Section 6). Inset: Temperature-dependent in-plane magnetic penetration depth, $\lambda_{ab}(T)$.

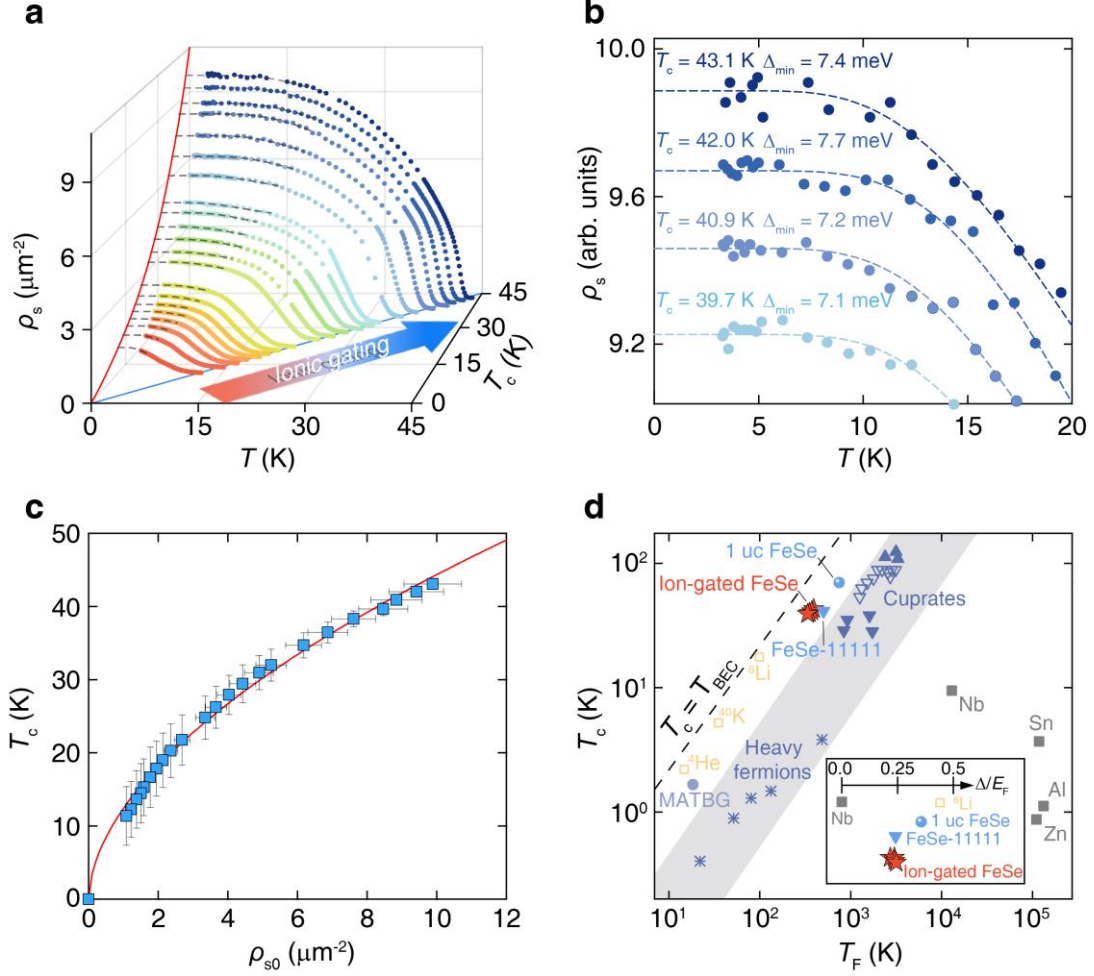


Fig. 2 | Evolution of the superfluid density in the ion-gated FeSe film. **a**, Temperature-dependent superfluid density, $\rho_s(T)$, for the ion-gated FeSe film with T_c systematically tuned from approximately 11 to 43 K. The dashed lines are the nodeless-gap fits to the first 10% drop in $\rho_s(T) / \rho_s(T \rightarrow 0)$, as depicted in the expanded view of the ρ_s data at low temperatures in **b**. **c**, Dependence of T_c on the zero-temperature superfluid density, $\rho_{s0} \equiv \rho_s(T \rightarrow 0)$, where ρ_{s0} is determined from the nodeless-gap fit. The definition of T_c is shown in Fig. 1c. The blue squares represent the experimental data; the red solid line is the fit to $T_c = \gamma \rho_{s0}^{0.55}$, where γ is the fit parameter. **d**, Uemura plot: T_c versus Fermi temperature, T_F , for various superconductors⁵⁰. The ion-gated FeSe with $T_c > 39$ K, as well as other FeSe-based superconductors, i.e., monolayer FeSe on SrTiO₃ substrate (1 uc FeSe) and (Li_{0.8}Fe_{0.2})OHFeSe (FeSe-1111) are located closer to the BEC limit for three-dimensional bosonic gas ($T_c = 0.218T_F$, the dashed line) than cuprate and heavy-fermion superconductors (the shade region). The large ratio of Δ/E_F

≈ 0.23 for ion-gated FeSe also indicates it lies in the BCS-BEC crossover regime (see the inset). T_F and E_F are obtained from ρ_{s0} using the formula given in Ref. ²⁸, i.e., $E_F = k_B T_F = \frac{\pi \hbar^2 d}{\mu_0 e^2} \rho_{s0}$, where d is the interlayer distance. The values of Δ are obtained from the nodeless-gap fits in **b**.

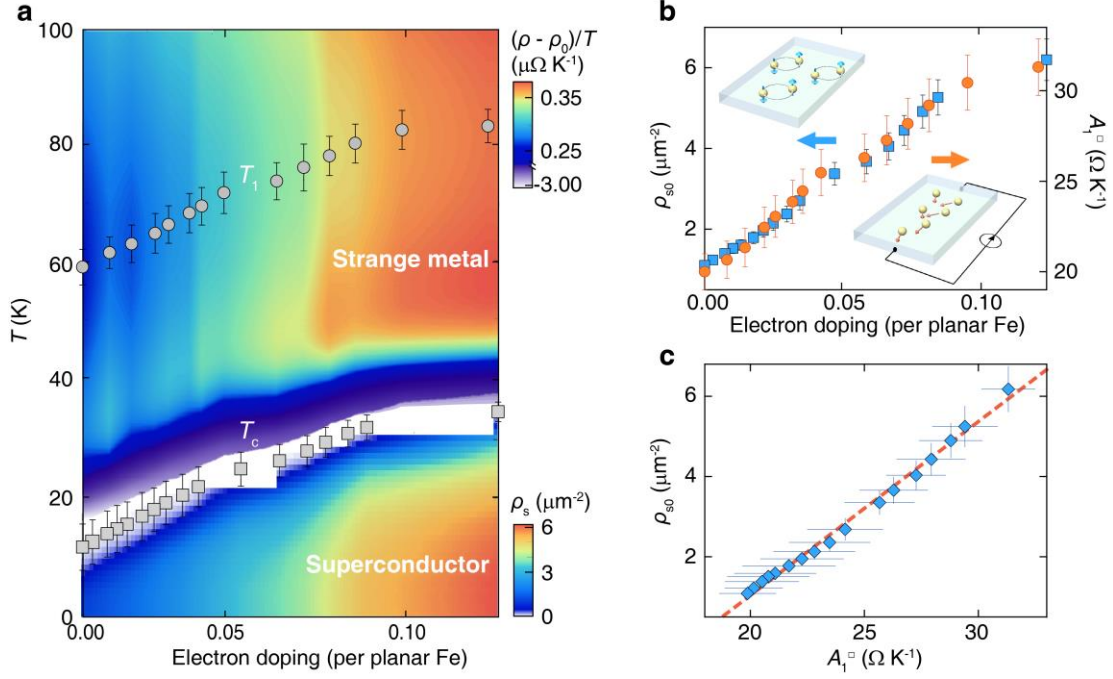


Fig. 3 | Correlation between unconventional superconductivity and the strange metallicity in the ion-gated FeSe film. **a**, Synchronized evolution of the strange-metal phase and the superfluid condensate with ionic-liquid gating. The strength of the strange-metal scattering, $(\rho - \rho_0)/T$, and the magnitude of the superfluid density, $\rho_s \equiv \lambda_{ab}^{-2}$, versus temperature T and election doping level are shown by the contour plot. The gray circles and gray squares represent the upper bound temperature of T -linear resistivity (T_1) and T_c , respectively. It is shown that the strange-metal phase [characterized by $(\rho - \rho_0)/T$ and T_1] and the superfluid condensate (characterized by ρ_s and T_c) changes synchronously with doping. Here ρ_0 is the residual resistivity obtained by fitting the resistivity at low temperatures (see the inset of Fig. S7) with the function $\rho = \rho_0 + A_1 T$. The normal state data are extracted from Fig. S8. The doping levels are extracted from the T_c versus doping relation in Ref. ¹⁰. **b**, The zero-temperature superfluid density, ρ_{s0} , (blue squares) and the T -linear coefficient per Fe-Se layer, A_1^\square , (red circles) versus electron doping in the ion-gated FeSe film. Here $A_1^\square = A_1/d_{\text{Fe-Se}}$, where $d_{\text{Fe-Se}}$ is the distance between adjacent Fe-Se layers. Evidently, ρ_{s0} tracks A_1^\square closely with electron doping, demonstrating a direct link between the formation of the superfluid in the ground state and the scattering or carriers in the strange-metal normal state. **c**, ρ_{s0} as a function of A_1^\square in the ion-gated FeSe film.

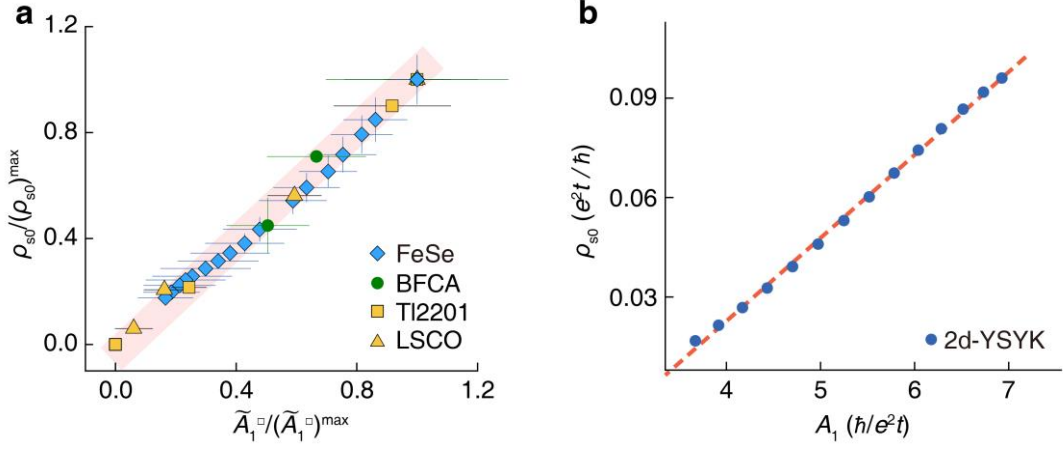


Fig. 4 | Scaling of the zero-temperature superfluid density and the T -linear resistivity coefficient for unconventional superconductors. a, Scaling of ρ_{s0} with \tilde{A}_1^{\square} for different superconducting systems, where ρ_{s0} and \tilde{A}_1^{\square} are normalized by their respective maximum values in the literature. Here, a constant has been subtracted from A_1^{\square} , namely $\tilde{A}_1^{\square} = A_1^{\square} - A_0$, where A_0 represents the non-zero extrapolation of A_1 to $T_c = 0$ K (Ref. ¹⁰). Data for $\text{Ba}(\text{Fe}_{1-x}\text{Co}_x)_2\text{As}_2$ (BFCA) are extracted from Refs. ^{9,30}. Data for $\text{Tl}_2\text{Ba}_2\text{CuO}_{6+\delta}$ (Tl2201) are obtained from Ref. ⁴⁰ and references therein. Data for heavily overdoped $\text{La}_{2-x}\text{Sr}_x\text{CuO}_4$ (LSCO, $T_c \leq 12$ K) are extracted from Refs. ^{10,18}. The error bars are reproduced from published data. The red shading is a guide to the eye. **b**, ρ_{s0} versus A_1 relation calculated based on the two-dimensional Yukawa-Sachdev-Ye-Kitaev (2d-YSYK) model (Supplementary Section 14), where \hbar is the reduced Planck constant and t is the fermion hopping.

References

- 1 Cooper, R. A. *et al.* Anomalous criticality in the electrical resistivity of $\text{La}_{2-x}\text{Sr}_x\text{CuO}_4$. *Science* **323**, 603-607 (2009).
- 2 Jin, K., Butch, N. P., Kirshenbaum, K., Paglione, J. & Greene, R. L. Link between spin fluctuations and electron pairing in copper oxide superconductors. *Nature* **476**, 73-75 (2011).
- 3 Licciardello, S. *et al.* Electrical resistivity across a nematic quantum critical point. *Nature* **567**, 213-217 (2019).
- 4 Lee, K. *et al.* Linear-in-temperature resistivity for optimally superconducting $(\text{Nd,Sr})\text{NiO}_2$. *Nature* **619**, 288-292 (2023).
- 5 Zhang, Y. *et al.* High-temperature superconductivity with zero resistance and strange-metal behaviour in $\text{La}_3\text{Ni}_2\text{O}_{7-\delta}$. *Nat. Phys.* (2024).
- 6 Zhu, Y. *et al.* Superconductivity in pressurized trilayer $\text{La}_4\text{Ni}_3\text{O}_{10-\delta}$ single crystals. *Nature* **631**, 531-536 (2024).
- 7 Cao, Y. *et al.* Strange metal in magic-angle graphene with near Planckian dissipation. *Phys. Rev. Lett.* **124**, 076801 (2020).
- 8 Patel, A. A., Guo, H., Esterlis, I. & Sachdev, S. Universal theory of strange metals from spatially random interactions. *Science* **381**, 790-793 (2023).
- 9 Yuan, J. *et al.* Scaling of the strange-metal scattering in unconventional superconductors. *Nature* **602**, 431-436 (2022).
- 10 Jiang, X. *et al.* Interplay between superconductivity and the strange-metal state in FeSe. *Nat. Phys.* **19**, 365-371 (2023).
- 11 Chen, L. *et al.* Shot noise in a strange metal. *Science* **382**, 907-911 (2023).
- 12 Keimer, B., Kivelson, S. A., Norman, M. R., Uchida, S. & Zaanen, J. From quantum matter to high-temperature superconductivity in copper oxides. *Nature* **518**, 179-186 (2015).
- 13 Putzke, C. *et al.* Reduced Hall carrier density in the overdoped strange metal regime of cuprate superconductors. *Nat. Phys.* **17**, 826-831 (2021).
- 14 Ayres, J. *et al.* Incoherent transport across the strange-metal regime of overdoped cuprates. *Nature* **595**, 661-666 (2021).
- 15 Greene, R. L., Mandal, P. R., Poniatowski, N. R. & Sarkar, T. The strange metal state of the electron-doped cuprates. *Annu. Rev. Condens. Matter Phys.* **11**, 213-229 (2020).
- 16 Taillefer, L. Scattering and pairing in cuprate superconductors. *Annu. Rev. Condens. Matter Phys.* **1**, 51-70 (2010).
- 17 Emery, V. J. & Kivelson, S. A. Importance of phase fluctuations in superconductors with small superfluid density. *Nature* **374**, 434-437 (1995).
- 18 Bozovic, I., He, X., Wu, J. & Bollinger, A. T. Dependence of the critical temperature in overdoped copper oxides on superfluid density. *Nature* **536**, 309-311 (2016).
- 19 Uemura, Y. J. *et al.* Universal correlations between T_c and n_s/m (carrier density over effective mass) in high- T_c cuprate superconductors. *Phys. Rev. Lett.* **62**, 2317-2320 (1989).
- 20 Hetel, I., Lemberger, T. R. & Randeria, M. Quantum critical behaviour in the superfluid density of strongly underdoped ultrathin copper oxide films. *Nat. Phys.* **3**, 700-702 (2007).
- 21 Leighton, C. Electrolyte-based ionic control of functional oxides. *Nat. Mater.* **18**, 13-18 (2019).
- 22 Lei, B. *et al.* Evolution of high-temperature superconductivity from a low- T_c phase tuned by carrier concentration in FeSe thin flakes. *Phys. Rev. Lett.* **116**, 077002 (2016).
- 23 Qin, M. *et al.* In situ magnetic measurements of ionic-liquid-gated superconducting films. *J.*

- Supercond. Nov. Magn.* **33**, 159-163 (2020).
- 24 Zuev, Y., Kim, M. S. & Lemberger, T. R. Correlation between superfluid density and T_c of underdoped $\text{YBa}_2\text{Cu}_3\text{O}_{6+x}$ near the superconductor-insulator transition. *Phys. Rev. Lett.* **95**, 137002 (2005).
- 25 Zhang, R. *et al.* Determining the absolute value of magnetic penetration depth in small-sized superconducting films. *Supercond. Sci. Technol.* **34**, 085022 (2021).
- 26 Hashimoto, K. *et al.* Microwave surface-impedance measurements of the magnetic penetration depth in single crystal $\text{Ba}_{1-x}\text{K}_x\text{Fe}_2\text{As}_2$ superconductors: Evidence for a disorder-dependent superfluid density. *Phys. Rev. Lett.* **102**, 207001 (2009).
- 27 Lin, H. T. *et al.* Determination of the London penetration depth of $\text{FeSe}_{0.3}\text{Te}_{0.7}$ thin films by scanning SQUID microscope. *Supercond. Sci. Technol.* **28**, 085006 (2015).
- 28 Shibauchi, T., Hanaguri, T. & Matsuda, Y. Exotic superconducting states in FeSe-based materials. *J. Phys. Soc. Jpn.* **89**, 102002 (2020).
- 29 Valdés Aguilar, R. *et al.* Pair-breaking effects and coherence peak in the terahertz conductivity of superconducting $\text{BaFe}_{2-2x}\text{Co}_{2x}\text{As}_2$ thin films. *Phys. Rev. B* **82**, 180514(R) (2010).
- 30 Williams, T. J. *et al.* Superfluid density and field-induced magnetism in $\text{Ba}(\text{Fe}_{1-x}\text{Co}_x)_2\text{As}_2$ and $\text{Sr}(\text{Fe}_{1-x}\text{Co}_x)_2\text{As}_2$ measured with muon spin relaxation. *Phys. Rev. B* **82**, 094512 (2010).
- 31 Dordevic, S. V. & Homes, C. C. Superfluid density in overdoped cuprates: Thin films versus bulk samples. *Phys. Rev. B* **105**, 214514 (2022).
- 32 Li, Z.-X., Kivelson, S. A. & Lee, D.-H. Superconductor-to-metal transition in overdoped cuprates. *npj Quantum Mater.* **6**, 36 (2021).
- 33 Lee-Hone, N. R., Dodge, J. S. & Broun, D. M. Disorder and superfluid density in overdoped cuprate superconductors. *Phys. Rev. B* **96**, 024501 (2017).
- 34 Kogan, V. G. Strong pairbreaking in anisotropic superconductors. *Phys. Rev. B* **81** (2010).
- 35 Homes, C. C. *et al.* A universal scaling relation in high-temperature superconductors. *Nature* **430**, 539-541.
- 36 Homes, C. C., Dordevic, S. V., Valla, T. & Strongin, M. Scaling of the superfluid density in high-temperature superconductors. *Phys. Rev. B* **72**, 134517 (2005).
- 37 Broun, D. M. *et al.* Superfluid density in a highly underdoped $\text{YBa}_2\text{Cu}_3\text{O}_{6+y}$ superconductor. *Phys. Rev. Lett.* **99**, 237003 (2007).
- 38 Franz, M. & Iyengar, A. P. Superfluid density of strongly underdoped cuprate superconductors from a four-dimensional XY model. *Phys. Rev. Lett.* **96**, 047007 (2006).
- 39 Sachdev, S. *Quantum phase transitions*. (Cambridge University Press, Cambridge, England, 1999).
- 40 Phillips, P. W., Hussey, N. E. & Abbamonte, P. Stranger than metals. *Science* **377**, eabh4273 (2022).
- 41 Hazra, T. a., Verma, N. a. & Randeria, M. Upper bounds on the superfluid stiffness and superconducting T_c : Applications to twisted-bilayer graphene and ultra-cold Fermi gases. Preprint at <https://arxiv.org/abs/1811.12428>.
- 42 Li, C. *et al.* Strange metal and superconductor in the two-dimensional Yukawa-Sachdev-Ye-Kitaev model. Preprint at <https://arxiv.org/abs/2406.07608>.
- 43 Hardy, A., Parcollet, O., Georges, A. & Patel, A. A. Enhanced strange metallicity from Coulomb repulsion. Preprint at <https://arxiv.org/abs/2407.21102>.
- 44 Tranquada, J. M., Lozano, P. M., Yao, J., Gu, G. D. & Li, Q. From nonmetal to strange metal at

- the stripe-percolation transition in $\text{La}_{2-x}\text{Sr}_x\text{CuO}_4$. *Phys. Rev. B* **109**, 184510 (2024).
- 45 Ye, S. *et al.* Emergent normal fluid in the superconducting ground state of overdoped cuprates. *Nat. Commun.* **15**, 4939 (2024).
- 46 Patel, A. A., Lunts, P. & Sachdev, S. Localization of overdamped bosonic modes and transport in strange metals. *Proc. Natl. Acad. Sci. USA* **121**, e2402052121 (2024).
- 47 Juskus, D., Ayres, J., Nicholls, R. & Hussey, N. E. Insensitivity of T_c to the residual resistivity in high- T_c cuprates and the tale of two domes. *Front. Phys.* **12**, 1396463 (2024).
- 48 Li, Q. *et al.* Prevailing Charge Order in Overdoped $\text{La}_{2-x}\text{Sr}_x\text{CuO}_4$ beyond the Superconducting Dome. *Phys. Rev. Lett.* **131**, 116002 (2023).
- 49 Sprau, P. O. *et al.* Discovery of orbital-selective Cooper pairing in FeSe. *Science* **357**, 75-80 (2017).
- 50 Nakagawa, Y. *et al.* Gate-controlled BCS-BEC crossover in a two-dimensional superconductor. *Science* **372**, 190-195 (2021).

Supplementary Information

Table of Contents

1. Film characterizations
2. Evolution of the normal-state carrier density with ionic-liquid gating
3. Device configuration and the in-situ TCMI measurement
4. Extracting the magnetic penetration depth using the FWC method
5. Evolution of the diamagnetic responses in the ion-gated FeSe film
6. Determining ρ_{s0} based on different gap symmetries
7. Failure of the dirty BCS model to account for the T_c versus ρ_{s0} scaling
8. Evolution of the electrical transport properties in the ion-gated FeSe film
9. Fitting the ρ_{s0} versus A_1^\square relation with error bars
10. Raw data shown in Fig. 3c
11. Correlation between ρ_{s0} and A_1^\square in other superconducting systems
12. ρ_{s0} versus A_1^\square relation in overdoped LSCO
13. Residual resistivity ratio of ion-gated FeSe and overdoped Tl2201
14. Two-dimensional Yukawa-Sachdev-Ye-Kitaev model
15. The residual T -linear resistivity term of overdoped cuprates

References

1. Film characterizations

To characterize the structural property of the film, we have performed the x-ray diffraction (XRD) measurements on FeSe films with two Ge (220) single crystals, as shown in Fig. S1. The XRD θ - 2θ scan pattern shows a high-quality (00 l) oriented growth (Fig. S1a), i.e., the ab plane is parallel to the film surface. The full width at half maximum (FWHM) of the XRD rocking curve is 0.477° , showing high crystalline quality (Fig. S1b). In addition, the high-quality epitaxy of the film is confirmed by a clear four-fold symmetry in the XRD ϕ scan pattern for the (011) diffraction peak (Fig. S1c). The c -axis lattice parameter calculated from the XRD θ - 2θ scan data by Bragg's law is 5.54 \AA , which is close to the 5.48 \AA of bulk FeSe (Ref. 1).

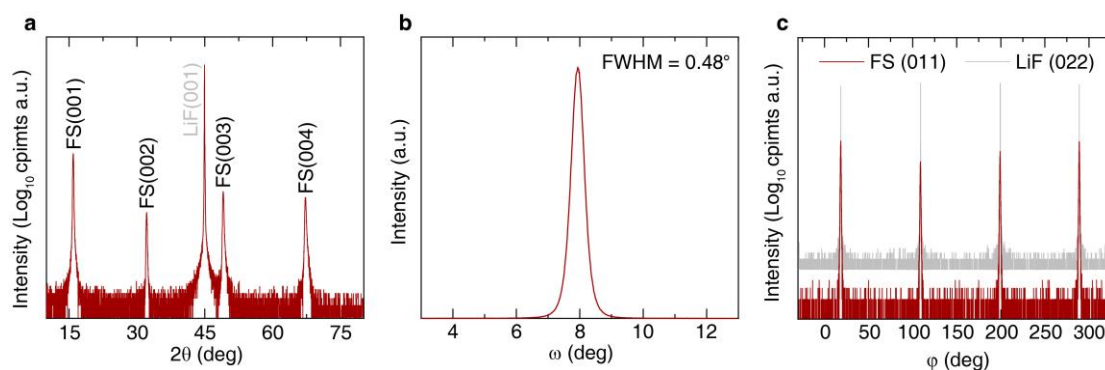


Fig. S1. XRD characterizations of a typical FeSe (FS) film grown on LiF substrate.

a, The θ - 2θ diffraction pattern. Only (00 l) peaks are observed for FeSe, indicating high crystallinity along the c -axis. **b**, The rocking curve of (001) peak, showing a narrow full width at half maximum (FWHM) of 0.48° . **c**, The ϕ -scan result of FeSe (011) and LiF (022) peaks, both of which show clear four-fold symmetry.

The chemical composition distributions of the film were characterized by the energy-dispersive x-ray (EDX) spectroscopy with a Hitachi SU5000 field-emission scanning electron microscope (SEM). Figure S2a shows a typical SEM micrograph of the film, showing a relatively flat surface. The averaged EDX spectrum of the image area is depicted in Fig. S2b. The EDX mappings of the image area are shown in Fig. S2c-d, demonstrating no signature of inhomogeneous compositional distributions on the micron scale.

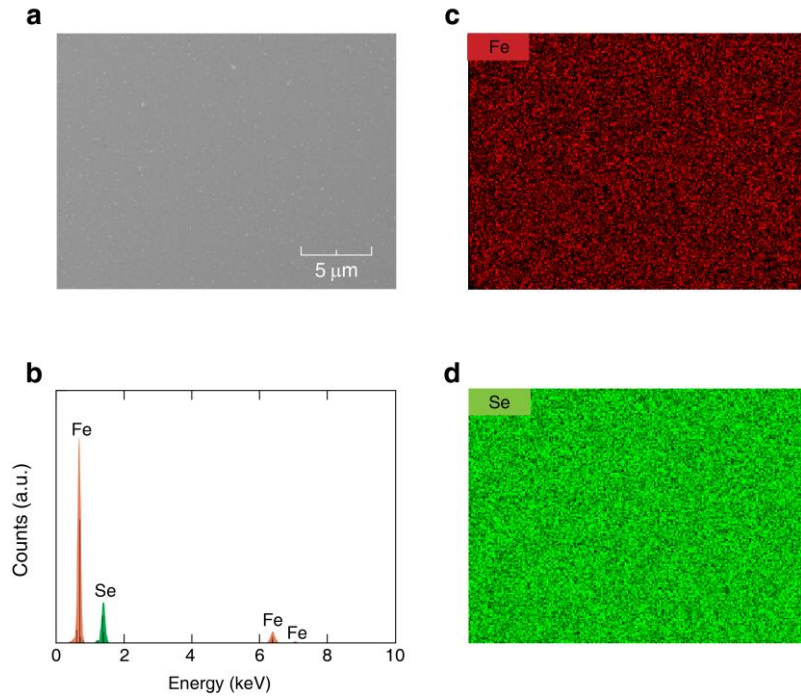


Fig. S2. EDX characterizations of a typical FeSe (FS) film grown on LiF substrate. **a**, SEM micrograph. **b**, EDX spectra for chemical compositions. **c-d**, EDX mappings corresponding to the SEM image area in **a**.

2. Evolution of the normal-state carrier density with ionic-liquid gating

FeSe is a multi-band system with hole pockets at Γ point and electron pockets at M point (see e.g., Ref. 2). With ionic-liquid gating, it was found that the hole density decreases and the electron density increases^{3,4}. Meanwhile, the superfluid density increases, as depicted in Fig. S3.

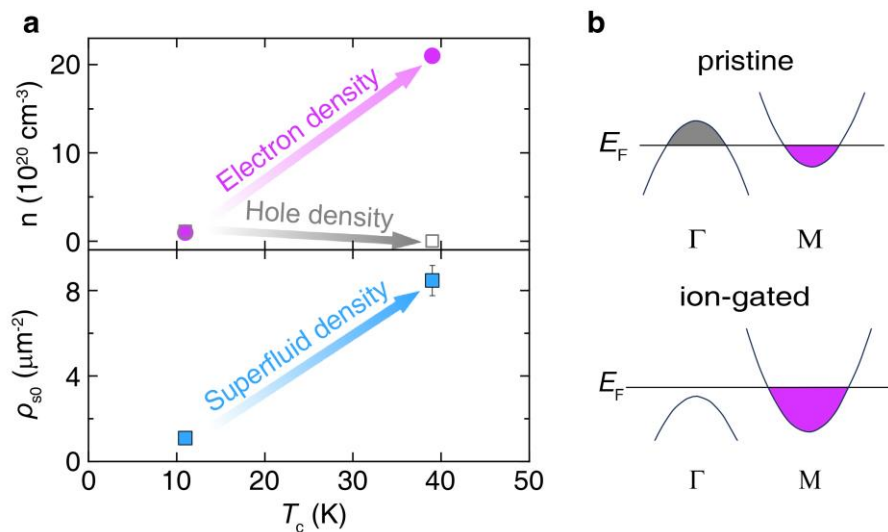


Fig. S3. a, Evolution of the normal-state carrier density and the superfluid density with

ionic-liquid gating. Data of the normal-state carrier density are obtained from Table. 1 in Ref. 4. **b**, Schematic illustrations of the band structure before (top) and after (down) ionic-liquid gating.

3. Device configuration and the in-situ TCMI measurement

Figure S4a shows a photograph of the ILG device. A FeSe/LiF film with size of $5 \times 5 \text{ mm}^2$ is placed next to a Si substrate covered by the SiO_2 insulating layer. A gate electrode with size of $10 \times 7 \text{ mm}^2$ is fabricated on the SiO_2 layer by depositing Au/Ti (50 nm/5 nm) with electron-beam evaporation. Electrical contacts are made by indium (In) soldering on the side of the FeSe film and a corner of the gate electrode. The ionic liquid DEME-TFSI is covered by a 6- μm -thick Kapton foil to confine its coverage on the sample and the gate electrode.

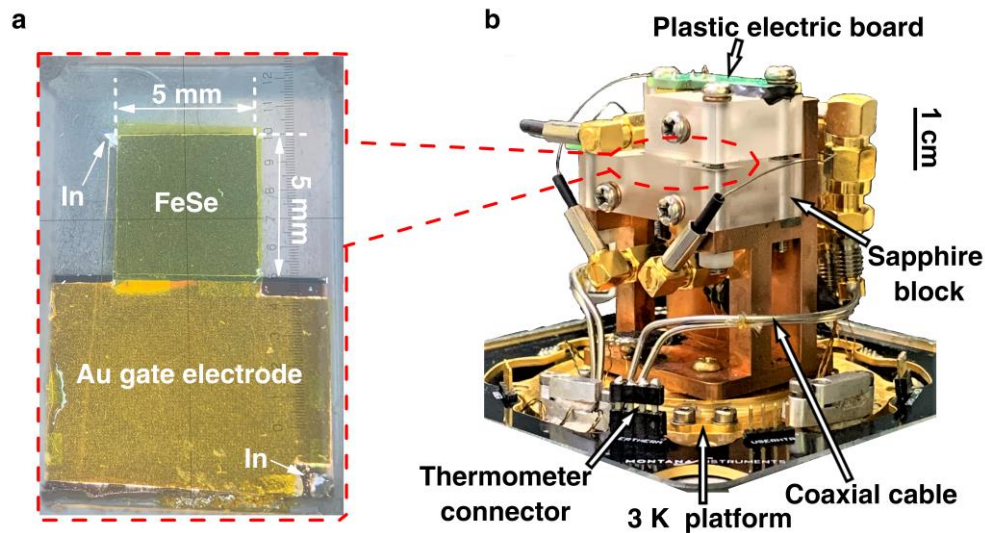


Fig. S4. Photographs of a, the ILG device and b, the TCMI apparatus. The ILG device is mounted inside the TCMI apparatus, indicated by the dashed line.

During the ionic-liquid gating, the ILG device is mounted inside a sapphire block of the TCMI apparatus (Fig. S4b). A drive coil and a pickup coil are sealed in the sapphire block with epoxy and aligned axially with the center of the FeSe film. The two coils are the same in size: The number of turns is 300, the inner diameter is 0.5 mm, the outer diameter is 1.3 mm, and the length is 1.6 mm. The pickup coil is pressed against the

backside of the LiF substrate, while the drive coil is about 0.4 mm away from the surface of the FeSe film. A plastic electric board is fastened on the sapphire block to provide a platform for wiring. To reduce noise and interference, coils are connected to coaxial cables. The apparatus is thermally connected to the 3 K platform of a Montana Instruments cryocooler. A Lakeshore thermometer is mounted inside the sapphire block to measure the sample temperature. A Keithley 2450 source meter is used to apply the gate voltage and monitor the leakage current. A Stanford Research SR830 lock-in amplifier is used to supply the alternating current to the drive coil. The current amplitude is 0.2 mA, and the frequency is 50 kHz, which is in the linear-response regime⁵. The induced pickup coil voltage, $V = V_x + iV_y$, is probed by the same lock-in amplifier with a reference phase of 90°.

A complete experiment includes a set of sequences, each of which involves 1) warming up to a target temperature (T_G) under a positive gate voltage (V_G), 2) staying at the target temperature for a given period of time (t_G), and 3) cooling down to measure the induced pickup coil voltage.

4. Extracting the magnetic penetration depth using the FWC method

Among various techniques for measuring the magnetic penetration depth⁶ (λ_{ab}), the TCMI technique has attracted increasing attention due to its high sensitivity, simplicity, and flexibility⁷⁻¹². A transmission-type TCMI system consists of a drive coil and a pickup coil, which are located on opposite sides of the superconducting film, as shown in Fig. 1a of the main text. A magnetic field is produced by the alternating current in the drive coil, inducing a voltage, $V = V_x + iV_y$, in the pickup coil. The real component, V_x , represents the inductive coupling, whereas the imaginary component, V_y , represents the resistive coupling.

When the films enter the Meissner state, two types of currents in the system will contribute to V_x . One is the alternating current applied to the drive coil, whose contribution can be calculated with the coil parameters based on classical electrodynamics. The other is the screening current induced in the superconducting film, which is related to λ_{ab} through¹³

$$\mathbf{j}_s(\mathbf{r}) + \frac{\sinh(d/\lambda_{ab})}{4\pi\lambda_{ab}} \int_{\Omega} d^2\mathbf{r}' \frac{\mathbf{j}_s(\mathbf{r}')}{|\mathbf{r} - \mathbf{r}'|} = -\frac{1}{\mu_0\lambda_{ab}^2} \mathbf{A}_d(\mathbf{r}), \quad (\text{S1})$$

where \mathbf{j}_s is the screening current density, Ω is the projection of the film on the x - y plane (film surface), $\mathbf{r} = \hat{\mathbf{x}}x + \hat{\mathbf{y}}y$, d is the film thickness, $\mu_0 = 4\pi \times 10^{-7} \text{ N A}^{-2}$ is the vacuum permeability, and \mathbf{A}_d is the vector potential generated by the drive current. Employing the FWC algorithm, Eq. S1 can be accurately solved and \mathbf{j}_s is obtained (Fig. 1b in the main text). Then the pickup coil voltage, V_{cal} , can be calculated by integrating the vector potential of both the drive and screening currents around each loop of the pickup coil. Finally, the absolute λ_{ab} can be extracted from a lookup table consisting of $V_{\text{cal}}/V_{\text{cal}}(T > T_c)$ for different λ_{ab} values. More details about this procedure can be found in Ref. 13.

5. Evolution of the diamagnetic responses in the ion-gated FeSe film

Figure S5 shows the raw TCM data used for determining the superfluid density in Fig. 2a of the main text. With ionic-liquid gating, T_c of the FeSe film is systematically tuned from approximately 8 to 43 K, reflecting as a continuous shift of the dip of the $V_y(T)$ curve. For each gated state, only a single magnetic transition is observed, confirming the bulk modulation of the superconductivity.

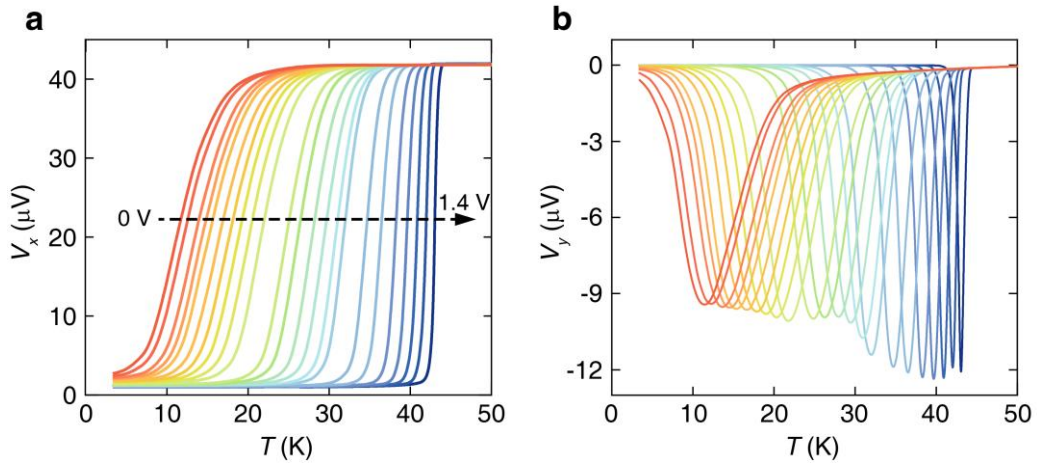


Fig. S5. Evolution of the diamagnetic responses in the ion-gated FeSe film. **a**, The real and **b**, the imaginary components of the pickup coil voltage, $V = V_x + iV_y$, as a function of temperature for successive gated states, respectively. From left to right, the gate voltages are $V_G = 0, 0.69, 0.7, 0.71, 0.73, 0.75, 0.76, 0.77, 0.78, 0.79, 0.8, 0.83$,

0.87, 0.91, 0.92, 0.97, 0.99, 1.06, 1.12, 1.18, 1.2, 1.4 V. $T_G \approx 325$ K and $T_G \approx 3$ h for each curve.

6. Determining ρ_{s0} based on different gap symmetries

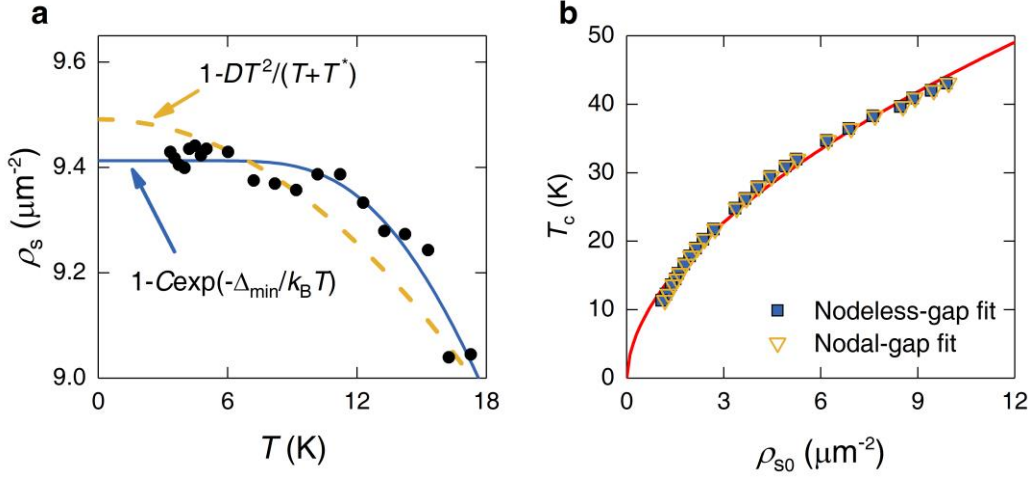


Fig. S6. Determination of the zero-temperature superfluid density, $\rho_{s0} \equiv \rho_s(T \rightarrow 0)$. **a**, Expanded view of the ρ_s data at low temperatures for the sample with $T_c \approx 42$ K. The solid and dashed lines denote the best fits using Eq. S2a and S2b to the first 10% drop of the $\rho_s(T)$ data, respectively. **b**, Dependence of T_c on ρ_{s0} , where ρ_{s0} is extrapolated using Eq. S2a (blue solid squares) and Eq. S2b (brown hollow triangles), respectively. The solid line indicates $T_c = \gamma \rho_{s0}^{0.55}$, as depicted in the main text.

To determine the extrapolated value of the zero-temperature superfluid density, $\rho_{s0} \equiv \rho_s(T \rightarrow 0)$, we have fitted the first 10% drop of the $\rho_s(T)$ data using the equations for nodeless-gap superconductors¹⁴

$$\rho_s(T)/\rho_{s0} = 1 - C \exp(-\Delta_{\min}/k_B T), \quad (\text{S2a})$$

and nodal-gap superconductors^{9,14,15}

$$\rho_s(T)/\rho_{s0} = 1 - D \frac{T^2}{T + T^*}, \quad (\text{S2b})$$

respectively. Here, Δ_{\min} is the minimum gap size at $T = 0$ K, k_B is the Boltzmann constant, C and D are fit parameters, and T^* represents the crossover temperature from quadratic to linear behavior. Figure S6a is an expanded view of the low-temperature behavior of ρ_s for a gated state with $T_c \approx 42$ K. It is shown that the nodeless-gap fit (the blue solid line) is in better agreement with our data, implying a nodeless pairing

gap in ion-gated FeSe. Nevertheless, the dependence of T_c on ρ_{s0} obtained with two gap symmetries are almost the same, as displayed in Fig. S6b.

7. Failure of the dirty BCS model to account for the T_c versus ρ_{s0} scaling

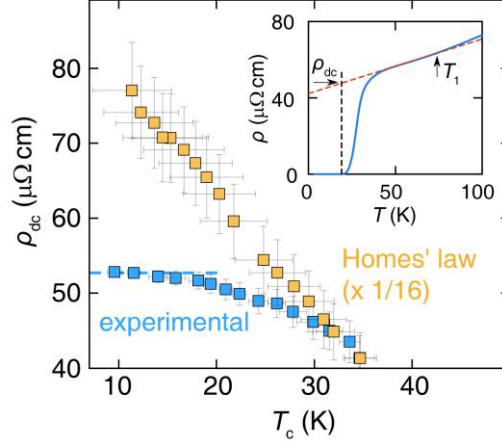


Fig. S7. Comparison of ρ_{dc} values calculated using Homes' law with measured values. The orange squares represent ρ_{dc} calculated from measured T_c and ρ_{s0} values by applying Homes' law (multiplied by 1/16), i.e., $\rho_{s0} \propto \sigma_{dc} T_c$, which follows from the Ferrell-Glover-Tinkham sum rule for dirty BCS superconductors. Blue squares are the ρ_{dc} obtained by extrapolating the T -linear resistivity, i.e., $\rho = \rho_0 + A_1 T$, above superconducting transition (the red dashed line) to T_c , as depicted in the inset. T_1 represents the upper bound temperature of T -linear resistivity. It is clear that ρ_{dc} calculated using Homes' law grows rapidly with T_c decreases, whereas the measured ρ_{dc} saturates when $T_c < 15$ K (see the blue dashed line).

8. Evolution of the electrical transport properties in the ion-gated FeSe film

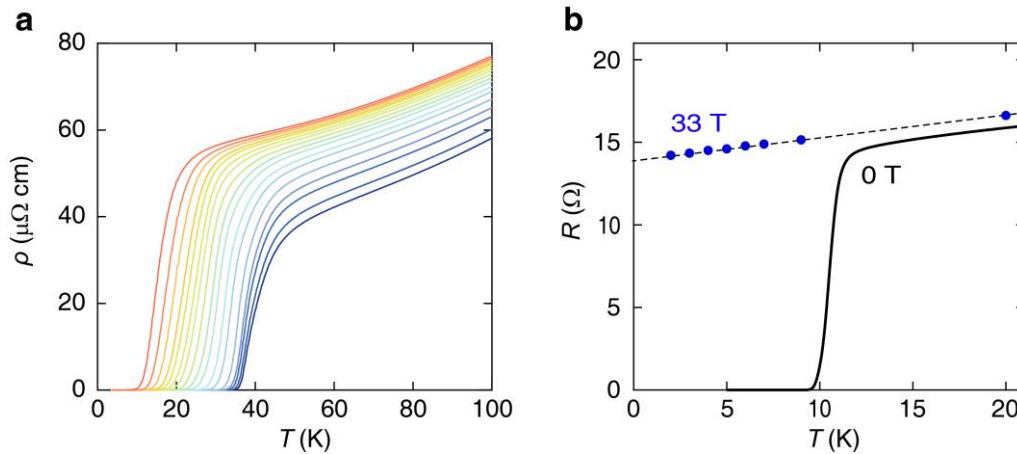


Fig. S8. Evolution of the electrical transport in the ion-gated FeSe film. a,

Temperature dependence of the resistivity for successive gating sequences. **b**, Temperature dependence of the resistance at zero field (solid line) and high field (33 T; blue dots). The black dashed line is a guide for T -linear resistivity. Data are extracted from our recent work¹⁶.

9. Fitting the ρ_{s0} versus A_1^\square relation with error bars

By fitting the data points in Fig. 3c together with the error bars using a more general power-law formula, i.e., $A_1^\square \sim \rho_{s0}^m$, the power-law exponent m is found to be 0.978 ± 0.063 , which is close to 1 and supports a linear relationship. We emphasize that the linear relationship is the most reasonable function to fit the data with the error bars taken into account. To further demonstrate this point, we present the fitting results using several common functions: root ($A_1^\square \sim \rho_{s0}^{1/2}$); linear ($A_1^\square \sim \rho_{s0}$); and quadratic ($A_1^\square \sim \rho_{s0}^2$) power-law dependences in Fig. S9. It is obvious that the data are in better agreement with the linear fit (Fig. S9b) than the root (Fig. S9a) and the quadratic (Fig. S9c) fits.

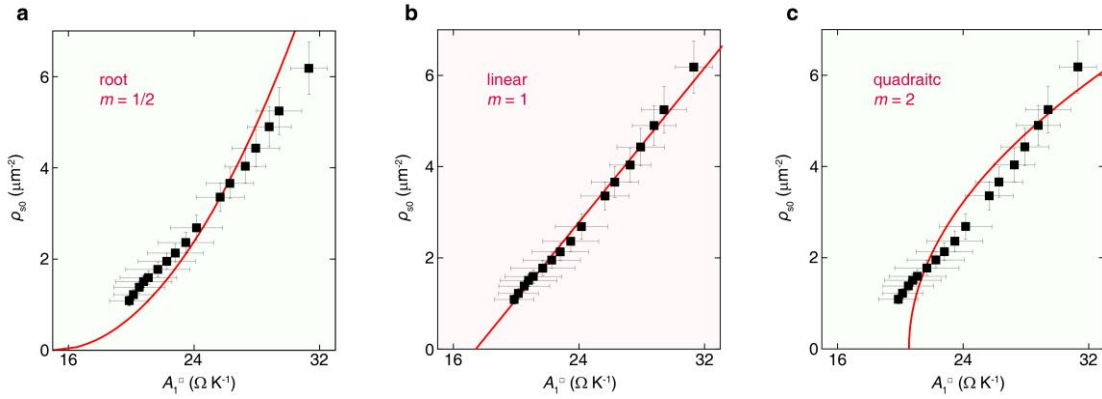


Fig. S9. Best fits of the ρ_{s0} versus A_1^\square data together with the error bars in Fig. 3b to **a**, root ($A_1^\square \sim \rho_{s0}^{1/2}$); **b**, linear ($A_1^\square \sim \rho_{s0}$); and **c**, quadratic ($A_1^\square \sim \rho_{s0}^2$) power-law dependences.

10. Raw data shown in Fig. 3c

Table S1. T-linear coefficients and zero-temperature superfluid density shown in Fig. 3c of the main text.

T_c (K)	A_1^\square ($\Omega \text{ K}^{-1}$)	ρ_{s0} (μm^{-2})
34.69	31.32	6.18
31.98	29.42	5.25
30.96	28.79	1.4
29.43	27.94	4.43
27.92	27.27	4.03
26.24	26.29	3.66
24.82	25.66	3.35
21.76	24.16	2.68
20.29	23.48	2.36
18.98	22.81	2.13
17.85	22.26	1.95
16.66	21.7	1.77
15.29	21.09	1.59
14.49	20.79	1.51
13.64	20.51	1.38
12.29	20.15	1.22
11.38	19.87	1.09

11. Correlation between ρ_{s0} and A_1^\square in other superconducting systems

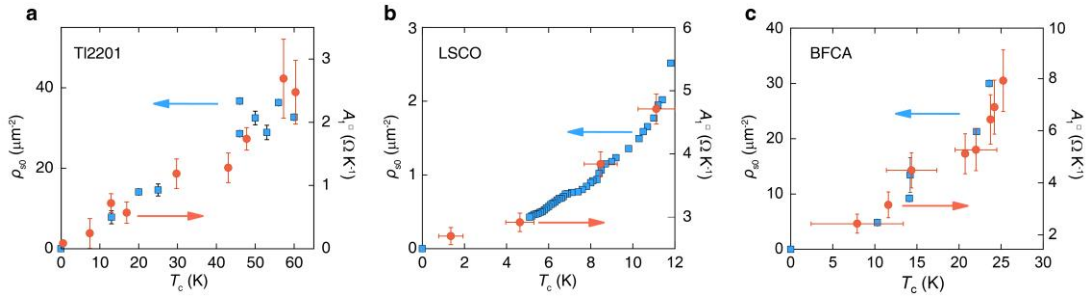


Fig. S10. Doping dependences of ρ_{s0} and A_1^\square in **a**, $\text{Tl}_2\text{Ba}_2\text{CuO}_{6+\delta}$ (Tl2201), **b**, $\text{La}_{2-x}\text{Sr}_x\text{CuO}_4$ (LSCO), and **c**, $\text{Ba}(\text{Fe}_{1-x}\text{Co}_x)_2\text{As}_2$ (BFCA). The T_c values correspond to different hole dopings for **a**, and **b**, and different cobalt concentrations for **c**. Data for Tl2201 are extracted from Ref. 17 and references therein; Data for LSCO are extracted from Refs. 9,16; Data for BFCA are extracted from Refs. 18,19.

12. ρ_{s0} versus A_1^\square relation in overdoped LSCO

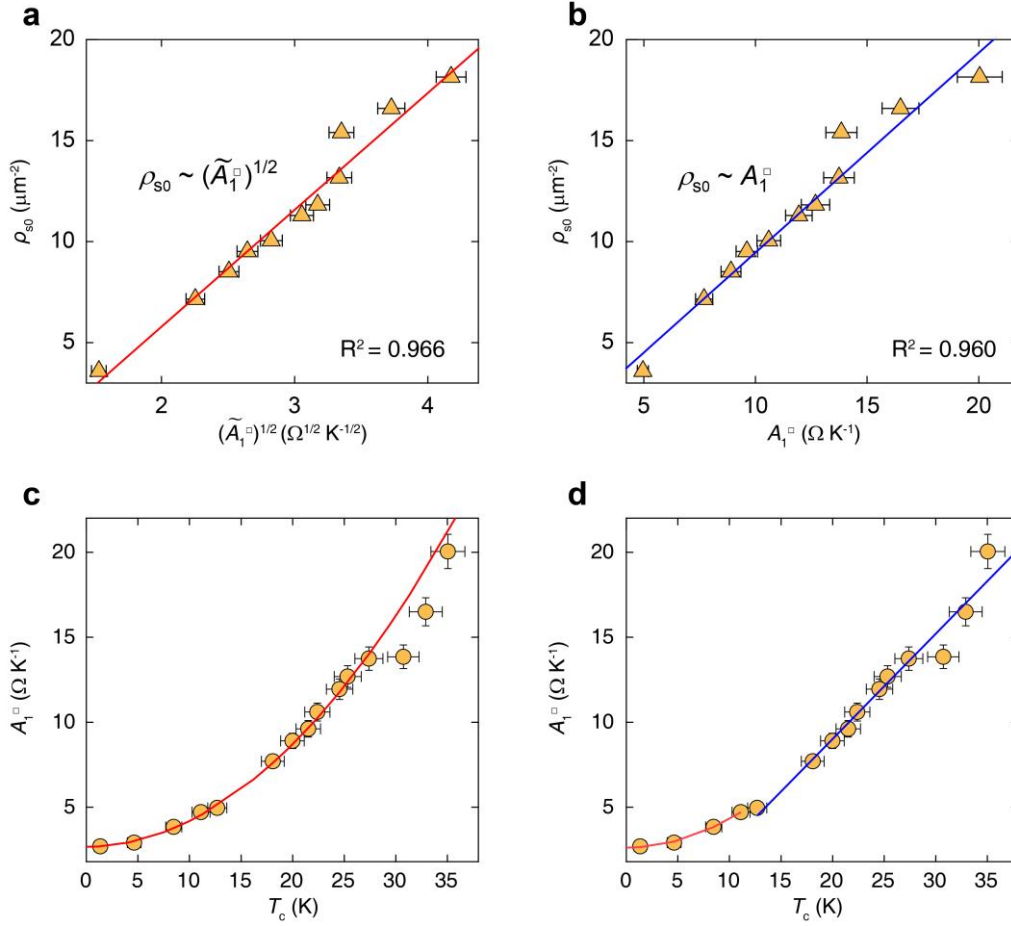


Fig. S11. Fitting the ρ_{s0} and A_1^\square relation for overdoped LSCO with $T_c > 12$ K using **a, $\rho_{s0} \sim (\tilde{A}_1^\square)^{1/2}$ and **b**, $\rho_{s0} \sim \tilde{A}_1^\square$.** It is noteworthy that the R-square (R^2) for two fits are almost equal, i.e., $R^2 = 0.966$ and 0.960 , respectively, indicating that a quantitative relation cannot be pinned down. This is due to the large uncertainty of the A_1^\square data for $T_c > 12$ K, where the fit of **c**, $T_c \sim (\tilde{A}_1^\square)^{1/2}$ or **d**, $T_c \sim A_1^\square$ [that is, similar to the behavior of $T_c(\rho_{s0})$ which changes from parabolic to linear relation as T_c exceed 12 K (Ref. 9)] are better remains unclear. Further studies are necessary to quantify the relation in this range. Data are obtained from Refs. 9,16.

13. Residual resistivity ratio of ion-gated FeSe and overdoped Tl2201

Figure S12 shows the evolution of $RRR = \rho(200 \text{ K})/\rho_0$ for ion-gated FeSe and overdoped Tl2201, both of which exhibit positive correlation with T_c , indicating that doping changes the amount of disorder in these systems. For FeSe, the disorder may relate to the Fe vacancy, of which the effects on transport and superconducting

properties were found to be suppressed by electron doping^{20,21}. For overdoped cuprates, it has been believed that the dopant ion serves as an intrinsic disorder (see e.g., Ref. 22).

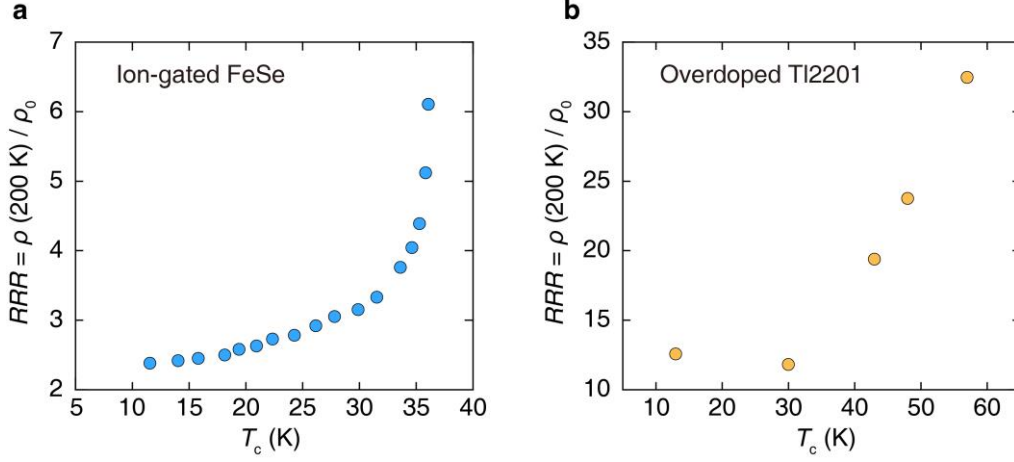


Fig. S12. Residual resistivity ratio of $RRR = \rho(200 \text{ K})/\rho_0$, where ρ_0 is obtained by fitting the resistivity above superconducting transition with $\rho = \rho_0 + A_1T$. **a**, Ion-gated FeSe film. **b**, Overdoped $\text{Tl}_2\text{Ba}_2\text{CuO}_{6+\delta}$ (Tl2201). The T_c values correspond to different electron dopings for **a**, and different hole dopings for **b**. Data for overdoped Tl2201 are obtained from Ref. 23 and references therein

14. Two-dimensional Yukawa-Sachdev-Ye-Kitaev model

This supplementary section will consider the 2d-YSYK model²⁴⁻²⁶ with the potential disorder v and the spatially random Yukawa coupling g' . We start with the imaginary time action

$$\begin{aligned}
S = & \int d\tau \sum_{\mathbf{k}, \sigma=\pm 1} \sum_{i=1}^N \psi_{i\mathbf{k}\sigma}^\dagger(\tau) [\partial_\tau + \epsilon(\mathbf{k})] \psi_{i\mathbf{k}\sigma}(\tau) + \frac{1}{2} \int d\tau \sum_{\mathbf{q}} \sum_{i=1}^N \phi_{i\mathbf{q}}(\tau) [-\partial_\tau^2 + \omega^2(\mathbf{q})] \phi_{i,-\mathbf{q}}(\tau) \\
& + \int d\tau d^2 r \sum_{i,j=1}^N \sum_{\sigma=\pm 1} \frac{v_{ij}(\mathbf{r})}{\sqrt{N}} \psi_{i\sigma}^\dagger(\mathbf{r}, \tau) \psi_{j\sigma}(\mathbf{r}, \tau) + \int d\tau d^2 r \sum_{i,j,l=1}^N \sum_{\sigma=\pm 1} \frac{g'_{ijl}(\mathbf{r})}{N} \psi_i^\dagger(\mathbf{r}, \tau) \psi_j(\mathbf{r}, \tau) \phi_l(\mathbf{r}, \tau),
\end{aligned} \tag{S3}$$

where the potential disorder v_{ij} and interaction disorder g'_{ijl} satisfy

$$\begin{aligned}
\overline{v_{ij}(\mathbf{r})} &= 0, & \overline{v_{ij}^*(\mathbf{r}) v_{i'j'}(\mathbf{r}') } &= v^2 \delta(\mathbf{r} - \mathbf{r}') \delta_{ii'} \delta_{jj'}, \\
\overline{g'_{ijl}(\mathbf{r})} &= 0, & \overline{g'_{ijl}^*(\mathbf{r}) g'_{i'j'l'}(\mathbf{r}') } &= g'^2 \delta(\mathbf{r} - \mathbf{r}') \delta_{ii'} \delta_{jj'} \delta_{ll'}.
\end{aligned} \tag{S4}$$

This was the model studied in Ref. 21, with an emphasis on the $v = 0$ case. The lattice dispersion is chosen as

$$\begin{aligned}\epsilon(\mathbf{k}) &= -2t(\cos k_z + \cos k_y) - \mu, \\ \omega^2(\mathbf{q}) &= m_b^2 + 2J(2 - \cos q_x - \cos q_y),\end{aligned}\tag{S5}$$

where t is the fermion hopping, μ is the chemical potential, m_b is the bare boson mass and J determines the boson dispersion.

A fixed length constraint

$$\sum_{\mathbf{q}} \sum_{i=1}^N \phi_{i\mathbf{q}}(\tau) \phi_{i,-\mathbf{q}}(\tau) = \frac{N}{\gamma},\tag{S6}$$

is included and the boson mass m_b is self-consistently determined for a fixed value of γ . We tune the scalar mass m_b away from the quantum critical point, and present our results in terms of the zero-temperature value of the renormalized boson mass $M^2 = m_b^2 - \Pi(\omega = 0, T = 0)$, where Π is the bosonic self-energy. The conductivity calculations^{26,27} yields the residual resistivity $\rho_0 \sim v^2$ and the linear-in- T slope $A_1 \sim g'^2$. Considering the fact that doping changes the amount of disorder (Fig. S6), we have also tuned the potential disorder v simultaneously. For all the results presented below, we fix the following parameters: $\sqrt{J}/t = 1$, $\mu/t = -0.5$, $g'/t^{3/2} = 5$. γ and v are chosen as

$$\begin{aligned}(1/\gamma)/t &= 0.19 - 0.00375(i - 1), \\ v/t &= 0.5 + 0.075(i - 1),\end{aligned}\tag{S7}$$

where i goes from 1 to 14.

Following the steps in Ref. 25, we obtain normal state resistivity ρ , the superconducting transition temperature T_c , and superfluid stiffness ρ_s . As shown in Fig. S13b, the dependence of T_c on ρ_{s0} exhibits a power-law behavior, $T_c \propto \rho_{s0}^{0.67 \pm 0.03}$, which shares similarities with the measurement $T_c \propto \rho_{s0}^{0.55 \pm 0.11}$ of ion-gated FeSe (Fig. 2c). The coefficient A_1 is extracted by fitting the T -linear resistivity in Fig. S13c with $\rho = \rho_0 + A_1 T$. We find superfluid stiffness ρ_{s0} can increase approximately linearly with the slope A_1 , as shown in Fig. 4b in the main text.

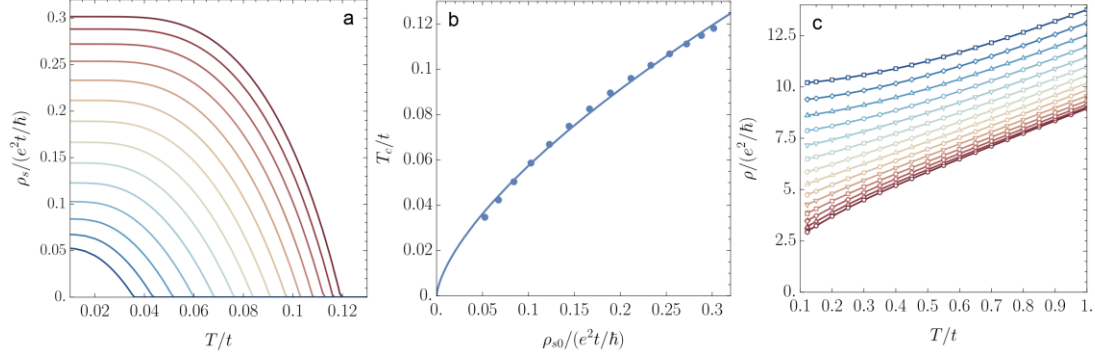


Fig. S13. Resistivity and superfluid stiffness in 2d-YSYK model. **a**, Temperature dependence of superfluid stiffness for different values of M/t . **b**, Dependence of T_c on the zero-temperature superfluid density, ρ_{s0} extracted from **a**. The solid line is the fit to $T_c = \gamma \rho_{s0}^{0.67}$. **c**, Normal state resistivity for varies M/t . In **a** and **c**, from dark red ($i = 1$) to dark blue ($i = 14$) the system is tuned away from the critical point, for $M/t = 0.4, 0.61, 0.79, 0.95, 1.1, 1.25, 1.39, 1.53, 1.67, 1.81, 1.95, 2.09, 2.23, 2.37$.

15. The residual T -linear resistivity term of overdoped cuprates

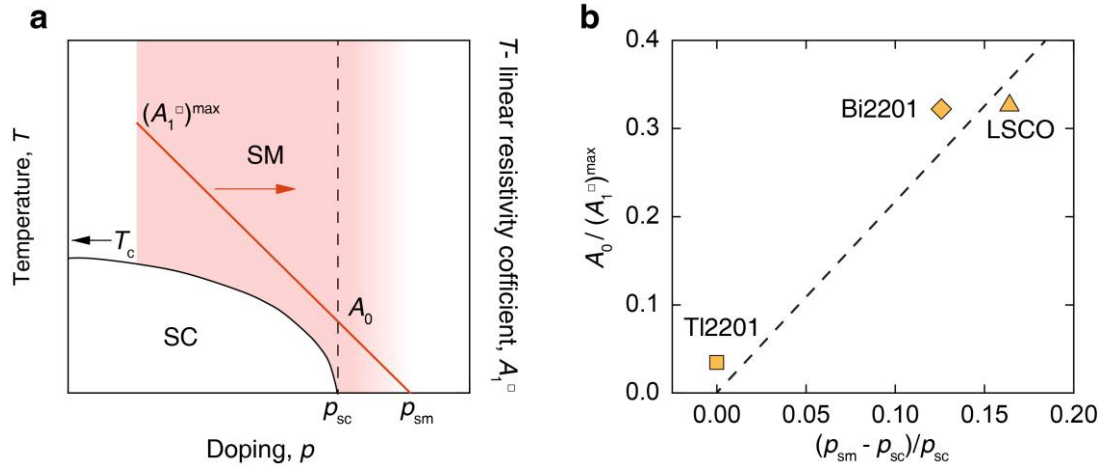


Fig. S14. Origin of the residual T -linear resistivity term for hole-doped cuprates. **a**, Schematic temperature versus doping phase diagram of overdoped cuprates. T_c is the onset temperature of the superconducting (SC) phase, A_1^\square is the T -linear resistivity coefficient of the strange-metal (SM) state. p_{sc} and p_{sm} represent the doping levels at which T_c and A_1^\square fade away, respectively. The mismatch between p_{sc} and p_{sm} results in a residual A_1^\square value (A_0) at the boundary of the SC dome. **b**, Dependence of A_0 on the mismatch between p_{sc} and p_{sm} for $\text{Ti}_2\text{Ba}_2\text{CuO}_{6+\delta}$ (Ti2201), $\text{Bi}_2\text{Sr}_2\text{CuO}_{6+\delta}$ (Bi2201), and

La_{2-x}Sr_xCuO₄ (LSCO). Data are obtained from Ref. 23.

References

- 1 Hsu, F.-C. *et al.* Superconductivity in the PbO-type structure α -FeSe. *Proc. Natl. Acad. Sci. USA* **105**, 14262-14264 (2008).
- 2 Sprau, P. O. *et al.* Discovery of orbital-selective Cooper pairing in FeSe. *Science* **357**, 75-80 (2017).
- 3 Lei, B. *et al.* Evolution of high-temperature superconductivity from a low- T_c phase tuned by carrier concentration in FeSe thin flakes. *Phys. Rev. Lett.* **116**, 077002 (2016).
- 4 Zhang, X. *et al.* Enhancement of electron correlations in ion-gated FeSe film by in situ Seebeck and Hall measurements. *Phys. Rev. B* **103**, 214505 (2021).
- 5 Zhang, R. *et al.* Measurement of magnetic penetration depth in superconducting films by two-coil mutual inductance technique. *Acta Phys. Sin.* **69**, 047401 (2020).
- 6 Prozorov, R. & Kogan, V. G. London penetration depth in iron-based superconductors. *Rep. Prog. Phys.* **74**, 124505 (2011).
- 7 Hebard, A. F. & Fiory, A. T. Evidence for the Kosterlitz-Thouless Transition in Thin Superconducting Aluminum Films. *Phys. Rev. Lett.* **44**, 291-294 (1980).
- 8 Logvenov, G., Gozar, A. & Bozovic, I. High-temperature superconductivity in a single copper-oxygen plane. *Science* **326**, 699-702 (2009).
- 9 Bozovic, I., He, X., Wu, J. & Bollinger, A. T. Dependence of the critical temperature in overdoped copper oxides on superfluid density. *Nature* **536**, 309-311 (2016).
- 10 Hetel, I., Lemberger, T. R. & Randeria, M. Quantum critical behaviour in the superfluid density of strongly underdoped ultrathin copper oxide films. *Nat. Phys.* **3**, 700-702 (2007).
- 11 Yao, G. *et al.* Diamagnetic response of potassium-adsorbed multilayer FeSe film. *Phys. Rev. Lett.* **123**, 257001 (2019).
- 12 Kinney, J., Garcia-Barriocanal, J. & Goldman, A. M. Homes scaling in ionic liquid gated La₂CuO_{4+x} thin films. *Phys. Rev. B* **92**, 100505(R) (2015).
- 13 Zhang, R. *et al.* Determining the absolute value of magnetic penetration depth in small-sized superconducting films. *Supercond. Sci. Technol.* **34**, 085022 (2021).
- 14 Skinta, J. A., Kim, M. S., Lemberger, T. R., Greibe, T. & Naito, M. Evidence for a transition in the pairing symmetry of the electron-doped cuprates La_{2-x}Ce_xCuO_{4-y} and Pr_{2-x}Ce_xCuO_{4-y}. *Phys. Rev. Lett.* **88**, 207005 (2002).
- 15 Hirschfeld, P. J. & Goldenfeld, N. Effect of strong scattering on the low-temperature penetration depth of a d-wave superconductor. *Phys. Rev. B* **48**, 4219-4222 (1993).
- 16 Jiang, X. *et al.* Interplay between superconductivity and the strange-metal state in FeSe. *Nat. Phys.* **19**, 365-371 (2023).
- 17 Phillips, P. W., Hussey, N. E. & Abbamonte, P. Stranger than metals. *Science* **377**, eabh4273 (2022).
- 18 Yuan, J. *et al.* Scaling of the strange-metal scattering in unconventional superconductors. *Nature* **602**, 431-436 (2022).
- 19 Williams, T. J. *et al.* Superfluid density and field-induced magnetism in Ba(Fe_{1-x}Co_x)₂As₂ and Sr(Fe_{1-x}Co_x)₂As₂ measured with muon spin relaxation. *Phys. Rev. B* **82**, 094512 (2010).
- 20 Chen, T. K. *et al.* Fe-vacancy order and superconductivity in tetragonal beta-Fe_{1-x}Se. *Proc. Natl.*

- Acad. Sci. U S A* **111**, 63-68 (2014).
- 21 Qin, M. *et al.* Granular metallicity as a minimal normal state for superconductivity. *Phys. Rev. B* **104**, 174511 (2021).
- 22 Tranquada, J. M., Lozano, P. M., Yao, J., Gu, G. D. & Li, Q. From nonmetal to strange metal at the stripe-percolation transition in $\text{La}_{2-x}\text{Sr}_x\text{CuO}_4$. *Phys. Rev. B* **109**, 184510 (2024).
- 23 Ayres, J. *et al.* Incoherent transport across the strange-metal regime of overdoped cuprates. *Nature* **595**, 661-666 (2021).
- 24 Esterlis, I., Guo, H., Patel, A. A. & Sachdev, S. Large- N theory of critical Fermi surfaces. *Phys. Rev. B* **103**, 235129 (2021).
- 25 Li, C. *et al.* Strange metal and superconductor in the two-dimensional Yukawa-Sachdev-Ye-Kitaev model. Preprint at <https://arxiv.org/abs/2406.07608>.
- 26 Patel, A. A., Guo, H., Esterlis, I. & Sachdev, S. Universal theory of strange metals from spatially random interactions. *Science* **381**, 790-793 (2023).
- 27 Aldape, E. E., Cookmeyer, T., Patel, A. A. & Altman, E. Solvable theory of a strange metal at the breakdown of a heavy Fermi liquid. *Phys. Rev. B* **105**, 235111 (2022).